Effective electrode design and reaction mechanism for electrochemical promotion of ammonia synthesis using Fe-based electrode catalysts

ARTICLE

Effective electrode design and reaction mechanism for electrochemical promotion of ammonia synthesis using Fe-based electrode catalysts

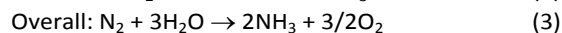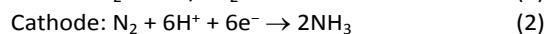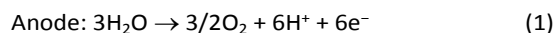Chien-I Li, Hiroki Matsuo and Junichiro Otomo*

The electrochemical promotion of ammonia formation on Fe-based electrode catalysts is investigated using proton-conducting-electrolyte-supported cells of H_2–Ar, Pt |$BaCe_{0.9}Y_{0.1}O_3$ (BCY)| Fe-based catalysts, H_2–N_2 at temperatures between 550˚C and 600˚C, and ambient pressure. To clarify the reaction mechanism, the ammonia formation rate is examined using two cathodes: (I) a porous pure Fe electrode with shorter triple phase boundary (TPB) length and (II) a cermet electrode consisting of Fe–BCY (or W–Fe–BCY) with longer TPB length. Using the different electrode structures, we investigate the effects of cathodic polarization, hydrogen partial pressure, and electrode material. The porous pure Fe electrode shows better performance than the Fe-BCY cermet electrode, which suggests that the ammonia formation is accelerated by the electrochemical promotion of catalysis (EPOC) effect on the Fe surface rather than the charge-transfer reaction at the TPB. The electrochemical promotion is governed by a dissociative mechanism, i.e., acceleration of direct N_2 bond dissociation with cathodic polarization on the Fe surface, with a smaller contribution by a proton-assisted associative mechanism at the TPB. These findings indicate that the porous pure Fe electrode is more effective for ammonia formation than the (W-)Fe–BCY cermet electrodes. Despite the relatively short TPB length, the porous pure Fe cathode achieves a very high ammonia formation rate of 1.4×10^{-8} mol cm^{-2} s^{-1} (450 µg h^{-1} mg^{-1}) under appropriate conditions. This significant result suggests that the effective double layer spreads widely on the Fe electrode surface. Using the identified reaction mechanism, we discuss key processes for improving ammonia formation.

Introduction

Ammonia is an essential product in our daily life, with millions of tons synthesized each year worldwide and the majority used as a nitrogen fertilizer for agriculture.[1] In addition to agriculture, ammonia is also a great candidate for chemical energy carrier of hydrogen because of its high hydrogen density of approximately 17.8% by weight.[2] Today, ammonia is industrially fabricated using the Haber–Bosch process, in which N_2 reacts with H_2 to form ammonia at high pressure and high temperature using iron-based catalysts.[3] However, in addition to its low energy efficiency, another challenging issue is that H_2 is commonly produced by methane steam reforming, which releases a large amount of carbon dioxide.[4] Therefore, there is growing interest in alternative and green processes for ammonia synthesis, especially by electrochemical reaction.[5-24] The advantages of the electrochemical synthesis of ammonia

include carbon-free emission,[25] decentralized production,[25] and higher energy efficiency.[26]

In the electrochemical synthesis of ammonia using proton-conducting electrolyte membrane, water dissociates to form protons at the anode (Eq. 1), and then the protons pass through the electrolyte membrane toward the cathode and react with nitrogen and electrons to form ammonia (Eq. 2). The overall reaction of ammonia formation is described in Eq. 3. Some previous studies replaced H_2 for H_2O in the anode to simplify the system and to investigate the N_2 reduction in the cathode.[5,6,8-11,15,16,21-23]

$$\text{Anode: } 3H_2O \rightarrow 3/2O_2 + 6H^+ + 6e^- \qquad (1)$$
$$\text{Cathode: } N_2 + 6H^+ + 6e^- \rightarrow 2NH_3 \qquad (2)$$
$$\text{Overall: } N_2 + 3H_2O \rightarrow 2NH_3 + 3/2O_2 \qquad (3)$$

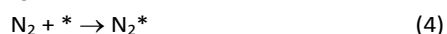The reaction mechanisms for ammonia electrochemical synthesis can be divided into two mechanisms, as described in Eqs. 4-9. For ammonia formation, N_2 and H_2 molecules adsorb on the catalyst surface and dissociate to form 2N* and 2H*, and then the adsorbates of H* and N* react to form NH_3.[27] In general, the reaction of N_2 dissociation is considered as the rate-determining step in ammonia formation.[28-33] To promote the electrochemical reaction of ammonia formation, appropriate catalysts,[34-37] and/or applying a voltage to accelerate the reaction of N_2 dissociation [11,15,24,36] were proposed. The reaction mechanism in N_2 dissociation was the same as that in the

Department of Environment Systems, Graduate School of Frontier Sciences, The University of Tokyo, 5-1-5 Kashiwanoha, Kashiwa-shi, Chiba 277-8561, Japan. E-mail: otomo@k.u-tokyo.ac.jp
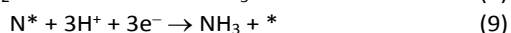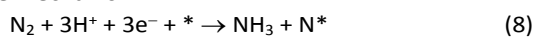
Haber–Bosch process with Fe catalyst, in which NH_3 formation reaction is followed by a dissociative mechanism (Eqs. 4–7). The rate-determining step is the dissociation of N_2^* into $2N^*$ on the catalyst surface (a two-phase boundary) (Eq. 5),[28-33] and the dissociated N^* then reacts with $3H^*$ to form NH_3. On the other hand, an alternative route of N_2 association to form NH_3 was also proposed.[38,39] First principles calculations based on density functional theory (DFT) have proposed that the associative mechanism (Eqs. 8 and 9), in which the adsorbed N_2^* reacts with protons and electrons to promote N_2 bond cleavage, with subsequent formation of NH_3 at the triple phase boundary (TPB) between the electrolyte, electrode, and gas phase (Eq. 8), can occur with cathodic polarization even at ambient temperature.[38,39]

Dissociative mechanism:

$$N_2 + * \rightarrow N_2^* \qquad (4)$$
$$N_2^* + * \rightarrow 2N^* \qquad (5)$$
$$H_2 + 2* \rightarrow 2H^* \qquad (6)$$
$$N^* + 3H^* \rightarrow NH_3 + 4* \qquad (7)$$

Associative mechanism:

$$N_2 + 3H^+ + 3e^- + * \rightarrow NH_3 + N^* \qquad (8)$$
$$N^* + 3H^+ + 3e^- \rightarrow NH_3 + * \qquad (9)$$

Many researchers have investigated the electrochemical reduction of N_2 to NH_3 at high temperature (>500°C) using a variety of catalysts including metals such as Fe,[11] Pd,[5] Ag,[17] Pt,[17] and AgPd[6,8-10], as well as cermet electrodes such as Ni–$BaCe_{0.2}Zr_{0.7}Y_{0.1}O_3$,[15,16,24] Ni–$BaCe_{0.9}Y_{0.1}O_3$,[23] Ru-doped $BaCe_{0.9}Y_{0.1}O_3$,[22] Ru-doped $La_{0.3}Sr_{0.6}TiO_3$[22], and K–Al–Fe–$BaCe_{0.9}Y_{0.1}O_3$.[21] Both noble metal[6-10] and ceramic catalysts result in similar ammonia formation rates of approximately 10^{-9} mol s^{-1} cm^{-2}.[15,16,24] The atmosphere in the cathode is another important factor affecting the ammonia formation rate. With the supply of pure N_2 to the cathode, some previous studies have shown that the mechanism of the electrochemical reduction of N_2 is initiated by pumped H^+ and dissociated N^* reacting with H^+ to form NH_3.[7,16,19] In addition, Kosaka et al. reported that the rate-determining step of N_2 dissociation can be accelerated by cathodic polarization using a Ru-based catalyst.[22] The hydrogen coverage surface at high applied voltage, however, hindered N_2 molecule adsorption and NH_3 formation. [11,13,18-20,22-24]

On the other hand, the ammonia electrochemical synthesis has also been investigated for the supply of a gaseous mixture of H_2–N_2 to the cathode.[11,15,16,21,24] Generally, the ammonia formation rate is higher than when pure N_2 is used because the H_2 in the cathode acts as an additional source of ammonia formation.[11,21] In that case, the ammonia formation rate can be enhanced by the electrochemical promotion of catalyst (EPOC) effect (i.e., non-Faradic process), which promotes the electron donation/backdonation reaction by an applied voltage.[11]

In our previous study, we also reported that the electrolyte-supported cell of H_2O–H_2–Ar, Pt |$BaCe_{0.9}Y_{0.1}O_3$ (BCY)| Al–K–Fe–BCY, N_2 exhibited a low electrochemical ammonia formation rate. Nevertheless, when a gaseous mixture of 15% H_2–85 %N_2 was supplied to the cathode side, there was a significant

increase in the ammonia formation rate from 2.8×10^{-11} to 6.7×10^{-10} mol s^{-1} cm^{-2}, which was observed with cathodic polarization at 650°C.[21] However, for a gaseous mixture of H_2–N_2 in the cathode, it is unclear whether the electrochemical promotion is caused by a dissociative mechanism (i.e., non-Faradic process without charge-transfer reaction), which accelerates N_2 dissociation on the Fe surface (Eq. 5), or a proton-assisted associative mechanism (i.e., Faradic process with charge-transfer reaction), which promotes the charge-transfer reaction of N_2^* at the TPB (Eq. 8).

In this study, the ammonia formation performance with cathodic polarization was examined using the following configuration of single cells: 3% H_2O–20% H_2–77% Ar, Pt |BCY| Fe-based catalysts, H_2–N_2. To investigate the electrochemical promotion of ammonia formation via either the dissociative or associative mechanism, a porous pure Fe cathode with relatively short TPB length (the relevant reactions are governed by a two-phase boundary, i.e., the Fe surface) and 10 wt.% Fe–BCY and 0.5 wt.% W–10 wt.% Fe–BCY cermet cathodes with relatively long TPB were used, as shown in Table 1. First, by comparing the 10 wt.% Fe–BCY cermet cathode (type A) with the porous pure Fe cathode (type B), the nature of the electrochemical promotion mechanism of ammonia formation was investigated. Second, a modified Fe–BCY cermet electrode, i.e., the same electrode structure as the type A but with the addition of W (type A'), was investigated. The exchange current density for H_2 evolution, $i_{0,H2}$, was low, and it could suppress the hydrogen evolution reaction and reduce the current density with cathodic polarization because of the higher adsorption energy of W–H formation relative to that of Fe–H.[40,41] Therefore, the effect of a low current density, i.e., low flux of pumped protons from the anode, on the electrochemical promotion of ammonia formation rate was also evaluated by comparing 10 wt.% Fe–BCY (type A) and 0.5 wt.% W–10% Fe–BCY (type A': x wt.% W–y wt.% Fe–BCY cathodes, where x and y represent the weight ratios of W and Fe, indicated by xw–yFe–BCY hereafter).

Table 1 Structure and properties of cathode catalysts

	Cathode	Electrode structure and property
Type A	Fe-BCY	Cermet electrode
		relatively long TPB length and high $i_{0,H2}$
Type A'	W-Fe-BCY	Cermet electrode
		relatively long TPB length and low $i_{0,H2}$
Type B	Fe	Porous Fe electrode
		relatively short TPB length and low $i_{0,H2}$
		Active site: Fe surface

Results and discussion

Characterization

Fig. 1 presents X-ray diffraction (XRD) patterns of the as-prepared samples for 10Fe–BCY (type A), porous pure Fe (type B), and 0.5W–10Fe–BCY (type A') cathodes on BCY electrolytes.
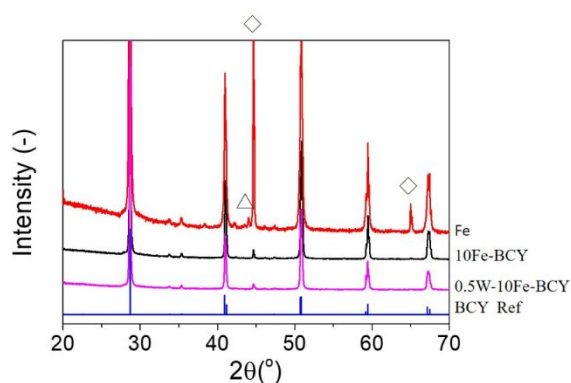
Fig. 1 XRD patterns for the as-prepared samples of 10Fe–BCY (type A), 0.5W–10F–BCY (type A'), and Fe (type B). ◇: Fe, △: Fe_3O_4. BCY reference: PDF#01-070-1429

The single phase of Fe (cubic, $Im\bar{3}m$, PDF#00-006-0696) and that of BCY originating from the BCY electrolytes appeared in all the samples. In the porous pure Fe cathode (type B), a partially oxidized Fe phase, Fe_3O_4, was observed due to the exposure of the sample to air. However, based on the result of the TG-DTA measurement (Fig. S1), the porous pure Fe cathode catalyst can maintain a pure Fe phase at the operating temperature (550°C). On the other hand, relevant peaks of W or W compounds were not detected because of the low amounts of W.

Fig. 2 shows cross-sectional scanning electron microscopy (SEM) images of the three cathode catalysts. The size of BCY particles was around 300 nm in pure BCY, 10Fe–BCY, and 0.5W–10Fe–BCY electrodes. Although it is difficult to distinguish each position of Fe particles in the 10Fe–BCY cathode from Fig. 2f, the deposition of Fe particles on BZY can be observed by TEM images (see next section). In 0.5W–10Fe–BCY cathode, Fe particles tend to aggregate on the BCY surface. In the porous pure Fe cathode, the size of Fe particles was around 200–400 nm. The thicknesses of the BCY and Fe porous cathodes were approximately 10–15 µm (see Fig. S2 in the supplementary information). Fig. 2i-k correspond to the SEM cross-sectional images of the cathodes after the electrochemical measurements. The particle aggregation of around 50, 130, and 150 nm were observed in 10Fe–BCY, 0.5W–10Fe–BCY, and porous pure Fe cathodes, respectively.

For further observation of the cathode structures of 10Fe–BCY and 0.5W–10Fe–BCY, transmission electron microscopy (TEM) was used to examine the detailed particle structures, as shown in Fig. 3. The TEM image of the pure porous BCY cathode showed that BCY particle size was around 300 nm. After Fe or W–Fe infiltrated into BCY, small particles located on the BCY surface were observed in 10Fe–BCY and 0.5W–10Fe–BCY cathodes. The energy-dispersive X-ray spectroscopy (EDX) mapping of 0.5W–10Fe–BCY showed that Fe signal around the
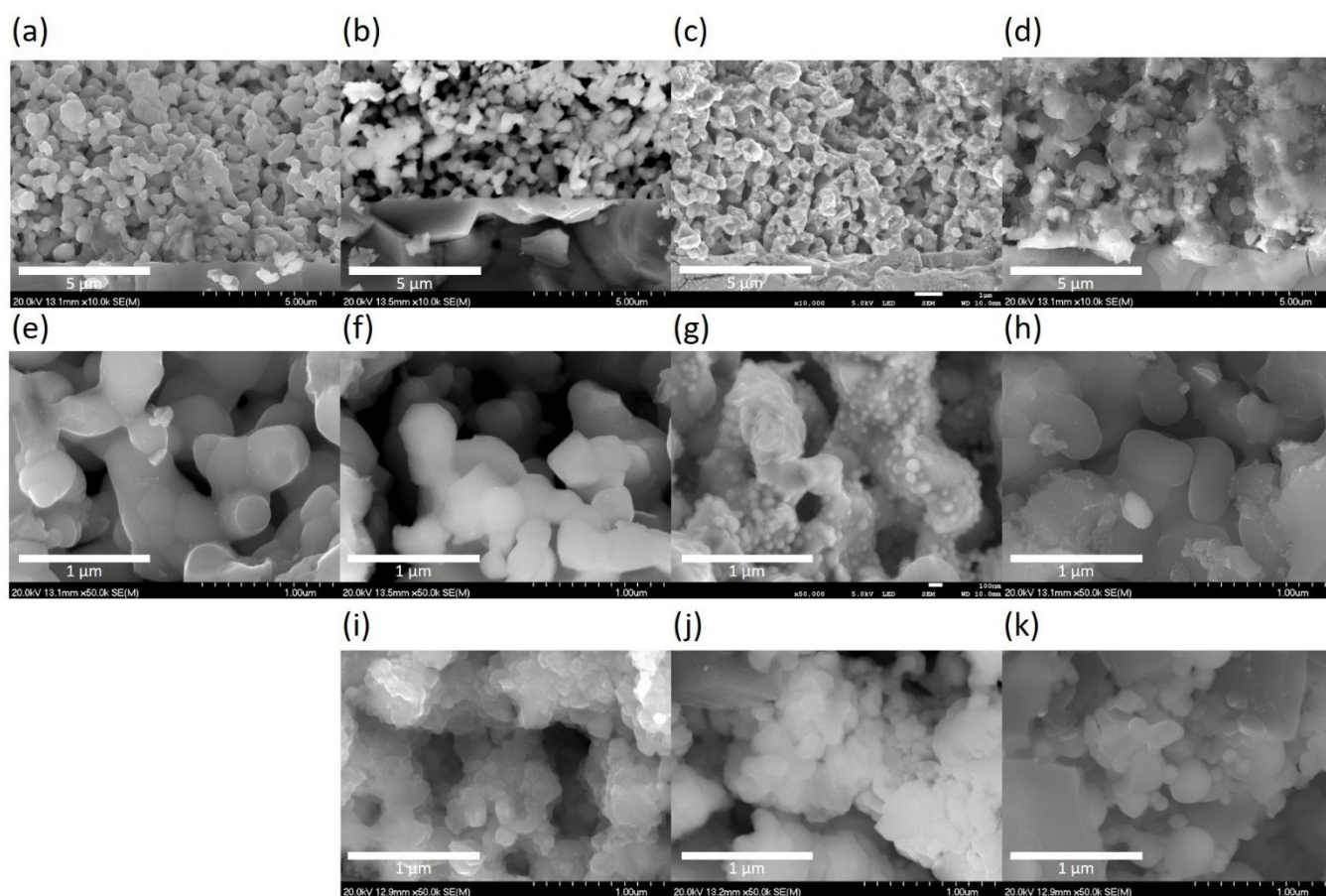
Fig. 2 Cross-section SEM images of (a), (e) pure BCY, (b), (f) as-prepared 10Fe–BCY (type A), (c), (g) as-prepared 0.5W–10Fe–BCY (type A'), (d), (h) as-prepared porous pure Fe (type B) cathodes, (i) 10Fe–BCY after electrochemical measurement, (j) 0.5W–10Fe–BCY after electrochemical measurement, and (k) porous pure Fe after electrochemical measurement.
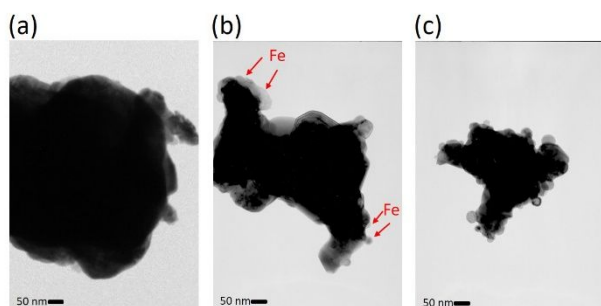
Fig. 3 TEM images of (a) pure BCY, (b) 10Fe–BCY for type A, and (c) 0.5W–10Fe–BCY for type A'.

Fig. 4 (a) TEM image of 0.5W–10Fe–BCY (type A') and EDX mapping for the elements (b) Fe, (c) Ce, and (d) W.

BCY surface was detected as well as Ce signal (Fig. 4). Judging from the TEM-EDX, we think that the small particles located on the BCY surface in Fig. 3b are Fe particles. However, because the W amount is too low to detect and the EDX peaks of W (M_α and M_β edges) and Y (L_α edge) are overlapping, we could not confirm the exact W position.

Electrochemical reaction of ammonia synthesis with different cathode structures

Fig. 5 shows the ammonia formation performance using 10Fe–BCY (type A), 0.5W–10Fe–BCY (type A'), and porous pure Fe (type B) cathodes in $10\%H_2$–$90\%N_2$. The broken lines are the ammonia formation rates at equilibrium. The ammonia formation rates at equilibrium change with the electrode potential because H_2 partial pressure in the cathode increased by the H_2 evolution reaction (Eq. 10). Here, we assume the current efficiency of H_2 evolution reaction is 100%. Therefore, an increase in H_2 partial pressure, Δp_{H2}, can be obtained by Eq. 11.

$$2H^+ + 2e^- \rightarrow H_2 \tag{10}$$

$$\Delta p_{H2} = \frac{i \times A \times R \times T}{n \times F \times v} \tag{11}$$

where i, A, R, T, n, F, and v are the current density, electrode area, gas constant, temperature, electron transfer number, Faraday constant, and flow rate in the cathode, respectively. The ammonia formation rates increased by approximately 30 times or more with cathodic polarization for the three cathode catalysts in comparison with that at the rest potential. The type A cell with 10Fe–BCY cermet cathode exhibited an ammonia formation rate of 4.2×10^{-10} mol s^{-1} cm^{-2} (101 µg h^{-1} mg^{-1} Fe), and the corresponding current density reached 0.055 A cm^{-2} at 600°C and -0.7 V. Thus, ammonia formation and hydrogen evolution proceeded in parallel with cathodic polarization.

With W addition to 10Fe–BCY, the type A' cell 0.5W–10Fe–BCY cathode exhibited a higher ammonia formation rate of 5.7 $\times 10^{-10}$ mol s^{-1} cm^{-2} at -1.2 V (137 µg h^{-1} mg^{-1} Fe) even at a lower operating temperature (550°C) than that of the 10Fe–BCY cathode. In addition, current density for type A' (0.5W-10Fe-BCY) cathode, i.e., proton flux from the counter electrode (anode) to the working electrode (cathode), was reduced by
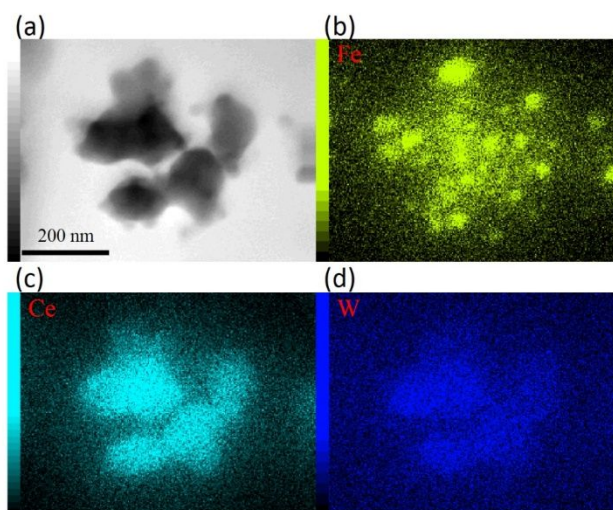
approximately 40% in comparison with that of type A (10Fe–BCY) cathode.

As for the exchange current density, the exchange current densities at 600°C for type A (10Fe–BCY) and type A' (0.5W–10Fe–BCY) were 0.037 and 0.014 A cm^{-2}, respectively. The reason for the low exchange current densities for 0.5W–10Fe–BCY was due to the suppression of hydrogen evolution reaction. Although the highest voltage of -1.5 V was applied for both the cathodes at 600°C, the ammonia formation rates for both the cathodes were mostly the same, whereas 0.5W–10Fe–BCY had a lower current density than that of 10Fe–BCY. Therefore, the results suggest that the influence of applied voltage on ammonia formation is more significant than that of current density.

When using the type B cell with porous pure Fe cathode, the ammonia formation rate increased with increasing cathodic polarization and reached 1.3 × 10^{-9} mol s^{-1} cm^{-2} (44.33 µg h^{-1} mg^{-1} Fe) at 550°C, which was the best performance of these three cathodes. Because the type B of porous pure Fe possessed a shorter TPB length than the type A of 10Fe–BCY, a low current density of approximately 0.03 A cm^{-2} at around -1.2 V was observed. As for the exchange current density, the exchange current density at 600°C for type B was 0.017 A cm^{-2}, which was also lower than that for type A due to the shorter TPB length in type B.

The current efficiency η_{CE} (Eq. 12) and the fraction of obtained NH_3 concentration to NH_3 concentration at equilibrium X_{Equ} (Eq. 13), using the 10Fe–BCY, 0.5W–10Fe–BCY, and porous pure Fe cathodes, were examined, as discussed in section 3 in the supplementary information (Fig. S3).

$$\eta_{CE} = \frac{r_{NH3} nF}{i} \tag{12}$$

$$X_{Equ} = \frac{p_{NH3} \text{ in the cathode}}{p_{NH3} \text{ at equilibrium}} = \frac{\dfrac{r_{NH3} \times A \times R \times T}{v}}{K \times p_{H2}^{\frac{3}{2}} \times p_{N2}} \tag{13}$$

where p_{NH3}, r_{NH3}, K, p_{H2}, and p_{N2}, are the ammonia partial pressure, ammonia formation rate, equilibrium constant for Eq.
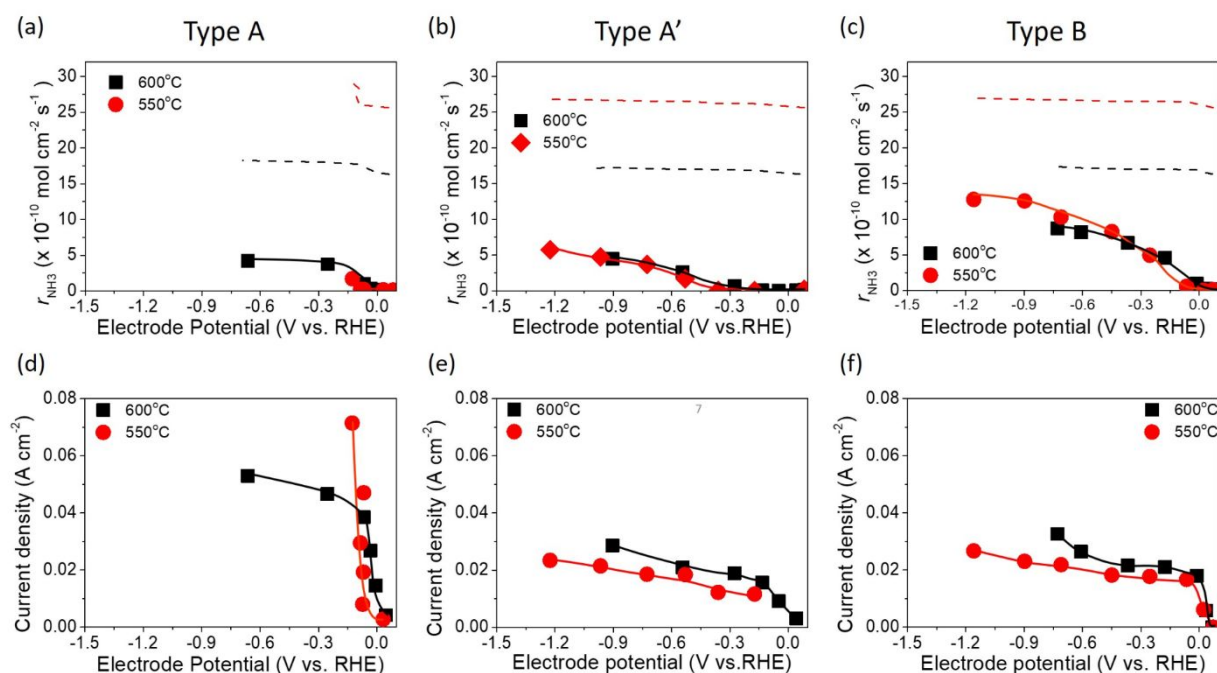
Fig. 5 Ammonia formation rates for (a) 10Fe–BCY (type A), (b) 0.5W–10Fe–BCY (type A'), and (c) porous pure Fe (type B) cathodes. The broken lines corresponded to the ammonia formation rates in thermodynamic equilibrium. Current densities for (d) 10Fe–BCY (type A), (e) 0.5W–10Fe–BCY (type A'), and (f) porous pure Fe (type B) cathodes.

14, hydrogen partial pressure, and nitrogen partial pressure, respectively.

$$N_2 + 3/2H_2 \rightarrow NH_3 \qquad (14)$$

The electrochemical ammonia synthesis involved the electrochemical synthesis of ammonia and hydrogen evolution reaction in parallel. According to Fig. S3, the current efficiency for NH_3 formation was below 2%, which implied that the hydrogen evolution reaction was more favourable (Eq. 10) in the electrochemical reaction of ammonia synthesis.

Obtained X_{Equ} about 50% (equilibrant to 36.5 ppm NH_3) in type B of porous pure Fe was higher than that of 26% in type A or type A'. The best performance for ammonia formation rate was achieved using type B of porous pure Fe cathode, which had a relatively shorter TPB length than that of type A or type A' cermet electrodes.

Electrochemical reaction of ammonia synthesis at different H₂ partial pressures

The dependence of ammonia formation rate on H_2 partial pressure in the cathode was investigated using the type A 10Fe–BCY cathode, as shown in Fig. 6. The ammonia formation rate was improved upon increasing the H_2 partial pressure in the cathode; however, the current densities were mostly similar, indicating that ammonia formation is mainly affected by the H_2 reactant in the cathode. This result indicates that the ammonia formation rate has a positive correlation with H_2 partial pressures in the cathode. On the basis of this result, the ammonia formation at different hydrogen partial pressures in the cathode (10–75% H_2–90–25% N_2 with 40 sccm) was examined using the type B of porous pure Fe cathode, as shown in Fig. 7. With increasing H_2 partial pressure in the cathode, the ammonia formation rate increased by 6 times from 2.2×10^{-9} mol s^{-1} cm^{-2} in 10% hydrogen to 1.4×10^{-8} mol s^{-1} cm^{-2} in 50%

hydrogen at −1.2 V. The best performance of ammonia formation was obtained in 50% H_2–50% N_2 rather than at the nominal composition of 75% H_2–25% N_2 for ammonia formation. From the SEM image, the particle aggregation after the electrochemical reaction was observed, which caused the reduction of the surface area and the degradation of the catalyst. The degradation of the catalyst decreased the ammonia formation rate by 10–15% (Fig. S4). Despite the

Fig. 6 (a) Ammonia formation rates and (b) current densities obtained using 10Fe–BCY cathode (type A) at 600°C at different hydrogen partial pressures (pumped protons from the anode).
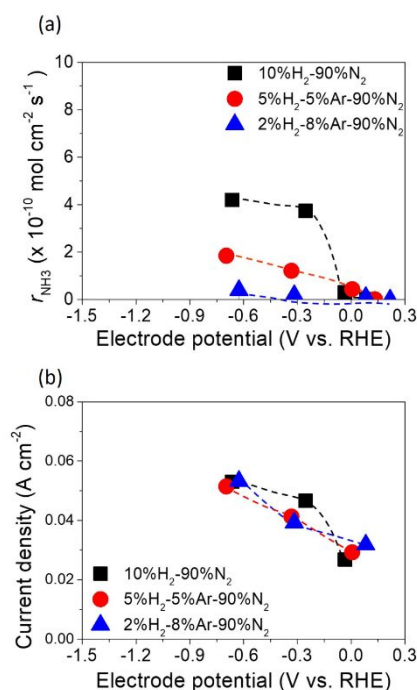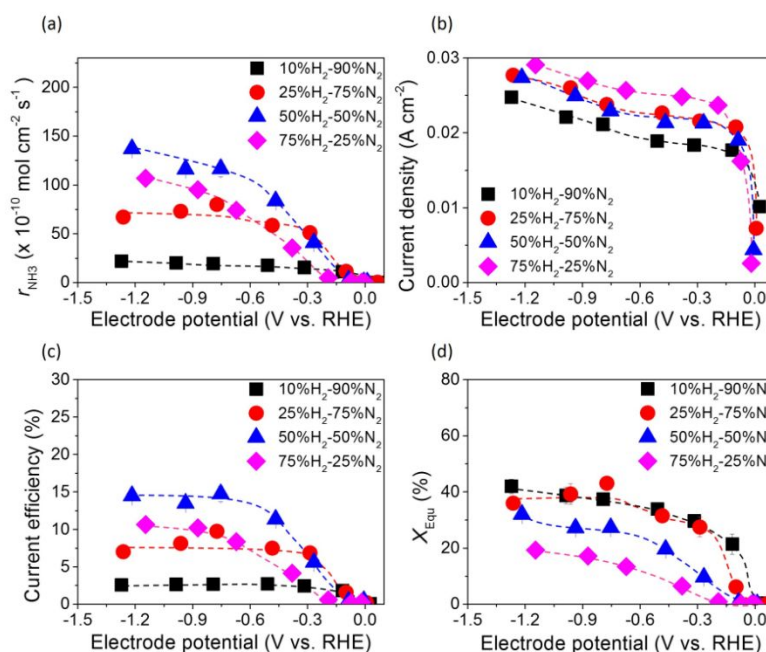
Fig. 7 (a) Ammonia formation rate, r_{NH3} (b) current density, (c) current efficiency, and (d) fraction of obtained NH$_3$ concentration to NH$_3$ concentration at equilibrium, X_{Equ}, at 550°C and 50% H$_2$–50% N$_2$ (40 sccm) obtained using pure Fe cathode.

degradation of catalyst, the ammonia formation rate in 50% H$_2$–50% N$_2$ was still higher than that in 75% H$_2$– 25% N$_2$.

Table S1 showed the observed ammonia partial pressure and theoretical ammonia partial pressures in the cathode at the different ratio of H$_2$ to N$_2$. X_{Equ} reached around 40% in 10% H$_2$–90% N$_2$, whereas it decreased to around 30% in 50% H$_2$–50% N$_2$ because the NH$_3$ partial pressure in 50% H$_2$–50% N$_2$ was higher than that in 10% H$_2$–90% N$_2$.

The ammonia formation rate increased by about 220 times to 1.4×10^{-8} mol s^{-1} cm^{-2} at around -1.2 V compared with that at rest potential. This result also confirms the conclusion that the ammonia formation rate has a strongly positive correlation with the H$_2$ partial pressure in the cathode. To the best of our knowledge, this ammonia formation rate of 1.4×10^{-8} mol s^{-1} cm^{-2} was quite high compared with the reported values in other existing electrochemical ammonia synthesis under moderate or ambient pressure. The representative previous studies are shown in Fig. 8, and the details are shown in Table S2 in the supplementary information.[11,16,21,42,43] Furthermore, the ammonia formation rate normalized by weight reached 450 μg h^{-1} mg^{-1}, which was much higher than those in other previous reports,[11,21,24,42,43] because the weight of Fe catalyst of 0.7 mg in this study was much less than that in the previous reports. Notably, the ammonia formation rate of 450 μg mg^{-1} h^{-1} at 550°C and 0.1 MPa is the similar level of the performance toward those of 250–976 μg mg^{-1} h^{-1} in the conventional Haber-Bosch process at 400°C and 7–10 MPa with Fe-based catalyst.[27] This result suggests that the Fe catalyst has significant performance in ammonia formation, and that Fe has the potential to be a cathode catalyst for ammonia electrochemical synthesis. To clarify the promotion of ammonia electrochemical synthesis using Fe cathode catalyst, the reaction mechanism is discussed in the next section.

Reaction mechanism

As described in the last section, our observations are summarized by the following four points: #1) The electrochemical promotion of ammonia formation was observed with cathodic polarization in a gaseous mixture of N$_2$–H$_2$ in the cathode, whereas a low ammonia formation rate (3×10^{-12} – 1.7×10^{-11} mol cm^{-2} s^{-1}) in pure N$_2$ even was detected upon an increase in the cathodic polarization for the type A
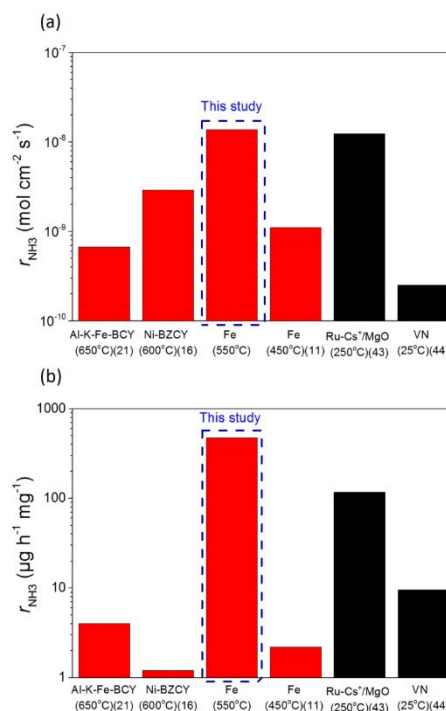
Fig. 8 Ammonia formation rates, r_{NH3}, were normalized by (a) area of electrode and (b) metal catalyst weight. The data in red and black were respectively obtained in H$_2$–N$_2$ and pure N$_2$ atmospheres.

ARTICLE

Table 2 Dissociative and associative mechanisms for ammonia formation[39, 44]

Dissociative mechanism		Associative mechanism	
$N_2 + * \rightarrow N_2*$	(R1)	$N_2* + H^+ + e^- \rightarrow N_2H*$	(R8)
$N_2* + * \rightarrow 2N*$	(R2)	$N_2H* + H^+ + e^- \rightarrow N_2H_2*$	(R9)
$H_2 + 2* \rightarrow 2H*$	(R3)	$N_2H_2* + H^+ + e^- \rightarrow N_2H_3*$	(R10)
$N* + H* \rightarrow NH* + *$	(R4)	$N_2H_3* \rightarrow N* + NH_3$	(R11)
$NH* + H* \rightarrow NH_2* + *$	(R5)	$N* + H^+ + e^- \rightarrow NH*$	(R12)
$NH_2* + H* \rightarrow NH_3* + *$	(R6)	$NH* + H^+ + e^- \rightarrow NH_2*$	(R13)
$NH_3* \rightarrow NH_3 + *$	(R7)	$NH_2* + H^+ + e^- \rightarrow NH_3*$	(R14)
		$NH_3* \rightarrow NH_3 + *$	(R15)

cathode (Fig. S5). #2) Infiltration of W into the Fe–BCY cermet electrode (type A' cathode) improved the ammonia formation rate because of the suppression of the hydrogen formation reaction and high cathodic polarization. #3) The performance of ammonia formation rate using the type B (pure Fe) electrode was better than that using the type A and A' cermet electrodes, although the TPB length in the type B cathode was short. #4) A strong correlation between the ammonia formation rate and hydrogen partial pressure in the cathode was observed. In this study, the highest ammonia formation rate, $>1.4 \times 10^{-8}$ mol s^{-1} cm^{-2}, was observed when the porous pure Fe cathode was used.

On the basis of the results, the details of the ammonia formation mechanism are discussed. In our system, both the dissociative mechanism (i.e., non-Faradic process without charge-transfer reaction) and proton-assisted associative mechanism (i.e., Faradic process with charge-transfer reaction) were possible routes for ammonia formation, as described in Table 2.

In the Haber–Bosch process, ammonia formation with an Fe-based catalyst is governed by a dissociative mechanism. The dissociative mechanism for ammonia formation on an iron catalyst has been extensively discussed in previous experimental and theoretical research.[45-50] For example, Ertl's group discussed the potential energy for the synthesis of ammonia over a potassium-promoted Fe catalyst based on the dissociative mechanism.[50] In addition, density functional theory (DFT) calculations were used to discuss a similar reaction mechanism.[45,47] The rate-determining step in the dissociative mechanism was considered to be dissociative chemisorption of N_2 on the Fe catalyst.[28-30] N_2 dissociation proceeded by electron donation from the Fe surface to the $N_2 \pi_{2p}*$ orbital, weakening the bonding of $N \equiv N$ and thus promoting N_2 cleavage directly (Eq. R2 in Table 2). In addition, a previous study showed that alkali metal (K) addition causes electron transfer from the alkali metal to the Fe catalyst, elevating the Fermi level of Fe and then

promoting the electron-backdonation reaction into $N_2 \pi_{2p}*$ and N_2 dissociation.[51]

However, N_2 dissociation cannot proceed easily at ambient temperature because of the insufficient energy to overcome the energy of N_2 dissociation. Previous DFT studies have shown that the electrochemical reaction of ammonia formation is dominated by a proton-assisted associative mechanism rather than a dissociative mechanism.[39] In the proton-assisted associative mechanism, protonation of adsorbed N_2* proceeds to form NH_3 and $N*$ without direct N_2 cleavage.

Generally, in SOFCs, relevant charge-transfer reaction proceeds at the TPB. If ammonia formation was governed by the proton-assisted associative mechanism, then the type A (10Fe–BCY) and type A' (0.5W–10Fe–BCY) cermet electrodes with relatively long TPB lengths should exhibit higher ammonia formation rates than the type B electrode. However, this hypothesis contradicts conclusion #3 stated above. In addition, according to conclusion #4 on the strong correlation between the ammonia formation rate and hydrogen partial pressure in the cathode, the ammonia formation process appears to be governed by the dissociative mechanism (Eqs. 4-7) rather than by the proton-assisted associative mechanism (Eqs. 8 and 9). In the final section, we discuss the mechanism of enhancement of the N_2 dissociation process on the Fe surface in terms of electrochemical promotion of the catalyst surface reaction.

Electrochemical promotion of catalyst effect and an effective double layer on Fe catalyst

Based on the results in the last section, the improvement of ammonia formation rate via the dissociative mechanism is probably caused by the electrochemical promotion of catalyst (EPOC) effect. Vayenas et al. proposed an EPOC effect model with cathodic or anodic polarization, in which the work function of metal catalyst could be changed and an effective double layer in a gas–solid system could be formed via spillover of mobile

ions originating from charge carriers in the electrolyte.[52] An increase or a decrease in metal work function could promote the electron donation/backdonation reaction. In our present system, the effective double layer can form on the Fe catalyst surface via H^+ spillover on the Fe surface, and the decrease in Fe work function can also promote electron backdonation, which can be induced by electron transfer from the Fe Fermi level to the N_2 antibonding orbital of π_{2p}^*, as shown in Fig. 9.[52] The EPOC effect can be described by Eq. 15:[52-56]

$$\ln\left(\frac{r_{NH3}}{r_{NH3,\,0}}\right) = \alpha_N \times \frac{\Delta\Phi}{k_b T} \qquad (15)$$

where $r_{NH3,0}$, α_N, $\Delta\Phi$, and k_b are the ammonia formation rate at rest potential, reaction constant, overpotential-induced change in the Fe work function, and Boltzmann's constant, respectively. According to the EPOC effect, the electrochemical promotion of ammonia formation is probably caused by N_2^* dissociation (R2), which is a rate-determining step for the dissociative mechanism. It is accelerated by the electron backdonation reaction with cathodic polarization, as shown in Fig. 9a. On the other hand, the effective double layer on Fe catalyst plays an important role in the electrochemical promotion of ammonia synthesis.

To support this hypothesis of the effective double layer, we conducted electrochemical ammonia synthesis using an yttria-stabilized zirconia (YSZ) electrolyte-based cell, which is an oxide ion conductor. The details of the experiment are described in the supplementary information (Section 7). Using the cell composed of 20% H_2–80% Ar, Pt |YSZ|10Fe-YSZ, 10% H_2–90% N_2, we did not observe any electrochemical promotion of the ammonia formation rate (Fig. S6). This suggests that the formation of the effective double layer with proton in the cathode plays an important role in the promotion of NH_3 formation reaction, as well as the cathodic polarization. Therefore, the structure of the effective double layer is very important and those of type A and type B are discussed in the last section.

Estimation of effective surface area and effective double layer

In the final section, we attempt to conduct an order-of-magnitude estimate of the effective surface area and discuss it through the comparison of type A (10Fe–BCY) and type B (pure Fe). According to the EPOC effect, the ammonia formation rate is proportional to the area of the reaction surface, i.e., the area of effective double layer, S^*_{eff}. Also, S_i (i denotes A and B for type A and type B, respectively) is defined as the total area of Fe particles connected with a network structure of electrons. The details of the definition and calculation for S^*_{eff}, S_A, and S_B are shown in the supplementary information (sections 8-10).

To understand the proton diffusion length and the area of the effective double layer, we propose three assumptions. #1. Proton diffusion length on the Fe surface is adequately long. Thus, we can assume that the Fe particles of type A can be covered by protons because the proton can fully diffuse on Fe particle surface of type A (the size of Fe particles on BCY in type A was around several tens of nanometer) and cover the Fe surface of type A to form an effective double layer (Fig. 9b).
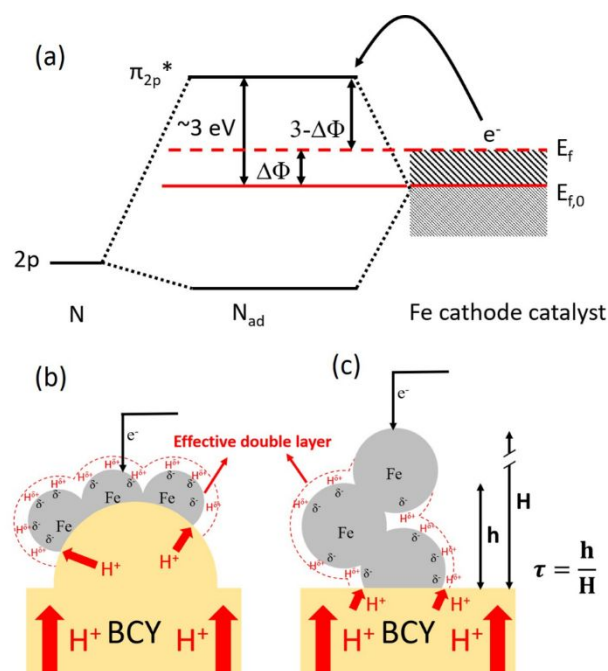
Fig. 9 (a) Energy diagram showing how N–N bonding was weakened by increasing the metal Fermi level with cathodic polarization. Schematic illustrations of effective-double-layer formation on the Fe surface in the (b) type A 10Fe–BCY and (c) type B porous pure Fe cathodes. H, h, and τ, are the electrode thickness, effective proton diffusion length, and ratio of the effective proton diffusion length to electrode thickness, respectively.

Therefore, the area of the effective double layer in type A, $S^*_{eff,A}$, is equal to the effective surface area of Fe particles, S_A (Eq. 16), as shown in Fig. 9b.

$$S^*_{eff,A} = S_A \qquad (16)$$

#2. In type B, the proton diffusion length, h, should be less than or equal to the thickness of the porous pure Fe cathode, H. The proton diffusion length could be represented as Eq. 17:

$$h = H \times \tau \qquad (17)$$

where τ is a constant between 0 and 1. Therefore, the effective double layer should be formed in a part of the porous pure Fe cathode via proton diffusion, as shown in Fig. 9c. The area of effective double layer in type B, $S^*_{eff,B}$, can be represented by the effective surface area of Fe particles multiplied with τ in type B (Eq. 18).

$$S^*_{eff,B} = S_B \times \tau \qquad (18)$$

#3. Because the electrochemical reaction of ammonia formation in type A and type B was carried out using Fe-based catalysts and at the same H_2 and N_2 partial pressures, the reaction rate constants for type A and type B were the same. The relation between the ammonia formation rate and the area of the effective double layer can be simplified as Eq. 19:

$$\left(\frac{r_{NH3,A}}{r_{NH3,B}}\right) = \frac{(S^*_{eff,A})}{(S^*_{eff,B})}$$
$$= \frac{(S_A)}{(S_B \times \tau)}, \qquad (19)$$

where $r_{NH3,A}$ and $r_{NH3,B}$, are the ammonia formation rates.

Supposed that the average values of the sizes of Fe particles in type A and type B were 42 nm and 190 nm, respectively, the corresponding effective proton diffusion length h was around 1.03 μm (Fig. 9c), the value of τ was about 0.08. Fig. S17 showed the details of the relationship among the effective proton diffusion length h, the size Fe particles in type A and B, and the porosity in type B. Therefore, the effective double layer can be formed on a part of the Fe electrode surface (1.03 μm distance from BCY electrolyte). The details of the estimation procedure of the effective double layer and the relevant parameters are summarized in the supplementary information (sections 11).

In conclusion, the present rough estimation of the effective surface area provides the following views: (I) protons diffusing from electrolyte can migrate to form an effective double layer (proton diffusion length: submicron order), and the effective double layer in type B (pure Fe) spreads adequately on Fe surface. (II) N_2 dissociation will be enhanced on the effective double layer via electron backdonation with cathodic polarization; thus, the improvement in ammonia formation rate was observed in type B.

In our present study, high ammonia formation rate in type B will be caused by the relatively large area of effective double layer. Our findings will aid in designing new reactors for the electrochemical synthesis of ammonia. To further improve ammonia formation rate, controlling the effective proton diffusion length in metal electrodes, designing relevant electrode structures, and reducing the operating temperature are particularly important. Design and optimization of the new reactor is our next challenge.

Conclusions

In this study, the ammonia formation rates of electrosynthesis using 10Fe–BCY, 0.5W–10Fe–BCY, and porous pure Fe cathodes were examined. The electrochemical promotion of ammonia formation in the three types of cathodes was dominated by the dissociative mechanism, with a smaller contribution by the proton-assisted associative mechanism.

At 550°C and 10% H_2–90% N_2 in the cathode, type A of 10Fe–BCY, which had relatively long TPB length, showed an ammonia formation rate of 4.2×10^{-10} mol cm^{-2} s^{-1}, while type A' of 0.5W–10Fe–BCY reduced the current density by 40% in comparison with type A of 10Fe–BCY, and it increased the ammonia formation rate to 5.7×10^{-10} mol cm^{-2} s^{-1}. These results suggest that the reduction of current density and the increase in cathodic polarization can contribute to an improved ammonia formation rate and current efficiency. On the other hand, type B of porous pure Fe, which had relatively short TPB length, exhibited a higher ammonia formation rate of 1.3×10^{-9} mol cm^{-2} s^{-1} than those of types A and A'. The high ammonia formation rate was probably achieved by accelerating N_2 dissociation on the Fe surface, i.e., dissociative mechanism, rather than that at TPB via proton-assisted associated mechanism with the charge-transfer reaction. Furthermore, with an increase in the H_2 partial pressure to 50% in the cathode, the significantly high ammonia formation rate, 1.4×10^{-8} mol s^{-1} cm^{-2} (450 μg h^{-1} mg^{-1}) at −1.2 V, was observed,

which was one of the best performance in the world. The electrochemical promotion of ammonia formation rate, which is higher by ca. 220 times as that at rest potential, will be caused by the EPOC effect rather than by the Faradaic electrochemical process, i.e., charge-transfer reaction at TPB. The results suggest that the formation of an effective double layer on Fe surface is very important for the ammonia formation process. Through the observations, the present work provides new strategies for designing efficient electrolysis cells for ammonia synthesis.

Experimental

Powder fabrication

$BaCe_{0.9}Y_{0.1}O_3$ (BCY) powder was synthesized by the coprecipitation method using precursors of $Ba(NO_3)_2$ (99.99% purity; Kanto Chemical Co., Inc., Japan), $Ce(NO_3)_3 \cdot 6H_2O$ (99.99% purity; Kanto Chemical Co., Inc., Japan), and $Y(NO_3)_3 \cdot 6H_2O$ (99.99% purity; Kanto Chemical Co., Inc., Japan), which were stoichiometrically dissolved in water. $(NH_4)_2(COO)_2$ (99.5% purity; Kanto Chemical Co. Inc., Japan), with concentration 1.5 times higher than the total cation concentration, was added as a precipitant. A white precipitate was obtained by filtering with suction filtration, and then dried at 80°C for one night. The dried precipitate was precalcined at 800°C and then calcined at 1200°C in air to obtain BCY powder. Finally, fine BCY powder was obtained by ball milling. Fine Fe_2O_3 powder (99.9% purity; Fujifilm Wako Pure Chemical, Co., Inc., Japan) was also obtained by ball milling.

Cell fabrication

Pelletized BCY was prepared by a uniaxial press and subsequent cold isostatic press. BCY powder (1.5 g) was first uniaxially pressed under 1 t cm^{-2}, and then isostatically pressed under 180 MPa. Next, the BCY pellets were calcined at 1600°C in air in a crucible with sacrificial powder of BCY to prevent intermixing and with vaporization of barium.

Porous pure Fe cathode (ca. 0.5 mg) on BCY electrolyte was prepared by the doctor-blade method. Fe_2O_3 powder was mixed with a slurry of α-terpineol (solvent) (98% purity; Fujifilm Wako Pure Chemical, Co., Inc., Japan), ethyl cellulose (binder) (48.0%–49.5% ethoxy content; Kanto Chemical, Co., Inc., Japan), Nonion OP-83 RAT sorbitan sesquioleate (dispersant) (NOF, Co., Japan), dibutyl phthalate (plasticizer) (99.5% purity; Kanto Chemical, Co., Inc., Japan), and poly(methyl methacrylate) resin (pore formation) (99.9% purity;: Tokyo Chemical Industry, Co., Ltd., Japan). The mixed slurry was then pasted onto the BCY electrolyte and calcined at 900°C in air to obtain a porous pure Fe cathode. A porous BCY (ca. 1 mg) electrode on BCY electrolyte was fabricated for the porous pure Fe cathode by the same process by using BCY powder.

In this paper, x wt.% W–y wt.% Fe–BCY cathodes (x and y are the weight ratios of W and Fe) are represented by xw–yFe–BCY. 10Fe–BCY and 0.5W–10Fe–BCY cathodes were fabricated by the impregnation method. Ammonium metatungstate (99.99% purity; Sigma-Aldrich, USA) and $Fe(NO_3)_3 \cdot 9H_2O$ (99.99% purity;

Journal Name

ARTICLE

Wako Chemical Co., Inc., Japan) were stoichiometrically dissolved in water. The mixture solution was poured onto the BCY porous cathode, and then annealed at 700°C to obtain the W–Fe–BCY cathode. The above processes were carried out several times until the amount of Fe and W reached an appropriate weight ratio. 10Fe–BCY cathode was fabricated using the same process as W–Fe–BCY except that only iron nitrate was used as a precursor and a lower annealing temperature of 500°C was applied. Pt counter electrode (CE) and Pt reference electrode (RE) for all pellets were attached on the opposite side of BCY electrolyte by the doctor-blade method. Finally, the obtained samples were then annealed at 900°C for 3h in 3% H_2, as shown in Fig. S18. Fig. S19 shows a schematic image of the three types of cathode structures.

Characterizations

All samples were characterized using scanning electron microscopy (SEM, JEOL JSM-5600, Japan), S4700 unit (Hitachi, Japan), X-ray diffraction (XRD, SmartLab, Rigaku, Japan), and transmission electron microscopy (TEM, JEOL JEM-1200EX, Japan and JEOL JEM-2010F, Japan). The Fe surface area in type B was detected by BET measurement (Nova 2200E, Quantachrome Instrument, USA)

Ammonia electrochemical synthesis

A single cell was set in between two quartz tubes in a furnace. Pyrex glass rings were used to seal the quartz tubes at 900°C. After sealing, Fe and Fe-W were reduced in 3% H_2/Ar and pure H_2 atmosphere, respectively. Then, the operating temperature was lowered to 550°C–600°C for ammonia electrosynthesis. Ammonia electrochemical synthesis was performed at different temperatures with a gaseous H_2–N_2 mixture introduced into the cathode and a gaseous 20% H_2–3% H_2O–77% Ar mixture introduced into the anode, as shown in Fig. S20.

AC impedance spectroscopic measurement from 1 to 10^6 Hz and potentiostatic measurement were performed using Autolab PGSTAT128N (Metrohm Autolab B.V., Netherlands). In the electrochemical measurements using the three-electrode method, the electrode potential, E, was defined as follows:

$$E = V_{app} - \left[IR_{ohm} + \frac{RT}{nF}\ln\left(\frac{p_{H2,anode}}{p_{H2,1bar}}\right) \right] \qquad (20)$$

$$\text{(i)} \qquad \text{(ii)}$$

where V_{app}, I, R_{ohm}, R, T, n, F, and p_{H2} are the applied voltage, current, ohmic resistance, gas constant, temperature, reaction electron number, Faraday constant, and H_2 partial pressure in the anode, respectively. The term (i) corresponds to IR loss correction, and (ii) is the term for correction of the potential difference between the H_2 partial pressure in the reference electrode and 1 bar H_2 pressure, i.e., standard pressure.

Ammonia formed in the cell was captured by allowing the outlet gas of the cathode side to flow into 0.01 mM H_2SO_4 solution, which was prepared by mixing ultrapure water (100 ml) (Autopure WT 100 compatible with Milli-Q, Yamato, Scientific Co., Ltd., Japan) and 0.005 M H_2SO_4 solution (0.1 ml) (Kanto Chemical, Co., Inc., Japan), for 5 min, and then the solution was analyzed by high performance ion chromatography (HPLC) (Extrema, Jasco, Japan).

A hydrogen pumping testing was also conducted using a single cell of 20% H_2–80% Ar, Pt |BCY| porous pure Fe, Ar. The current efficiency achieved 80-85% because the energy loss was probably caused by the leakage current (Fig. S21).

The blank test, ammonia deformation reaction test, and reversible test for ammonia electrochemical synthesis were discussed in the supplementary information (sections 13-15), respectively. The stability of porous pure Fe was examined in 10% H_2–90% N_2 in the cathode. The details were discussed in the supplementary information (section 16).

Conflicts of interest

The authors declare no conflict of interest.

Acknowledgements

References

1. J. W. Erisman, M. A. Sutton, J. Galloway, Z. Klimont, and W. Winiwarter, *Nature Geoscience,* **1** 636-639 (2008).
2. W. Wang, J. M. Herreros, A. Tsolakis, and A. P. E. York, *International Journal of Hydrogen Energy,* **38** (23), 9907-9917 (2013).
3. M. Appl, *Ammonia principles and industrial practice*, Wiley-VCH, Germany (1999).
4. S. Giddey, S. P. S. Badwal, C. Munnings, and M. Dolan, *ACS Sustainable Chemistry & Engineering,* **5** (11), 10231-10239 (2017).
5. G. Marnellos and M. Stoukides, *Science,* **282** 98-100 (1998).
6. Y. Xie, J.-D. Wang, R.-Q. Liu, X.-T. Su, Z.-P. Sun, and Z.-J. Li, *Solid State Ionics,* **168** (1-2), 117-121 (2004).
7. Z.-J. Li, R.-Q. Liu, J.-D. Wang, Y.-H. Xie, and F. Yue, *Journal of Solid State Electrochemistry,* **9** (4), 201-204 (2005).
8. J.-D. Wang, Y.-H. Xie, Z.-F. Zhang, R.-Q. Liu, and Z.-J. Li, *Materials Research Bulletin,* **40** (8), 1294-1302 (2005).
9. Z. Li, R. Liu, Y. Xie, S. Feng, and J. Wang, *Solid State Ionics,* **176** (11-12), 1063-1066 (2005).
10. F. Zhang, Q. Yang, B. Pan, R. Xu, H. Wang, and G. Ma, *Materials Letters,* **61** (19-20), 4144-4148 (2007).
11. M. Ouzounidou, A. Skodra, C. Kokkofitis, and M. Stoukides, *Solid State Ionics,* **178** (1-2), 153-159 (2007).
12. A. Skodra and M. Stoukides, *Solid State Ionics,* **180** (23-25), 1332-1336 (2009).

13. W. B. Wang, X. B. Cao, W. J. Gao, F. Zhang, H. T. Wang, and G. L. Ma, *Journal of Membrane Science,* **360** (1-2), 397-403 (2010).
14. I. A. Amar, R. Lan, C. T. G. Petit, V. Arrighi, and S. Tao, *Solid State Ionics,* **182** (1), 133-138 (2011).
15. E. Vasileiou, V. Kyriakou, I. Garagounis, A. Vourros, A. Manerbino, W. G. Coors, and M. Stoukides, *Topics in Catalysis,* **58** (18-20), 1193-1201 (2015).
16. E. Vasileiou, V. Kyriakou, I. Garagounis, A. Vourros, and M. Stoukides, *Solid State Ionics,* **275** 110-116 (2015).
17. D. S. Yun, J. H. Joo, J. H. Yu, H. C. Yoon, J.-N. Kim, and C.-Y. Yoo, *Journal of Power Sources,* **284** 245-251 (2015).
18. J. Otomo, N. Noda, and F. Kosaka, *ECS Transactions,* **68** (1), 2663-2670 (2015).
19. F. Kosaka, N. Noda, T. Nakamura, and J. Otomo, *Journal of Materials Science,* **52** (5), 2825-2835 (2016).
20. S. Kishira, G. Qing, S. Suzu, R. Kikuchi, A. Takagaki, and S. T. Oyama, *International Journal of Hydrogen Energy,* **42** (43), 26843-26854 (2017).
21. F. Kosaka, T. Nakamura, A. Oikawa, and J. Otomo, *ACS Sustainable Chemistry & Engineering,* **5** (11), 10439-10446 (2017).
22. F. Kosaka, T. Nakamura, and J. Otomo, *Journal of The Electrochemical Society,* **164** (13), F1323-F1330 (2017).
23. N. Simoda, Y. Kobayashi, Y. Kimura, G. Nakagawa, and S. Satokawa, *Journal of the Ceramic Society of Japan,* **125** (4), 252-257 (2017).
24. E. Vasileiou, V. Kyriakou, I. Garagounis, A. Vourros, A. Manerbino, W. G. Coors, and M. Stoukides, *Solid State Ionics,* **288** 357-362 (2016).
25. G. Centi, G. Iaquaniello, and S. Perathoner, *BMC Chemical Engineering,* **1** (1), (2019).
26. Julie N. Renner, Lauren F. Greenlee, Andrew M. Herring, and K. E. Ayers, *The Electrochemical Society Interface,* **24** (2), 51-57 (2015).
27. H. Liu, *Ammonia synthesis catalysts : innovation and practice*, World Scientific, Singapore (2013).
28. P. Stoltze and J. K. Nørskov, *Physical review letters,* **55** (22), 2502-2505 (1985).
29. P. Stoltze, *Physica Scripta,* **36** 824-864 (1987).
30. P. Stoltze and J. K. Nørskov, *Journal of Vacuum Science & Technology A: Vacuum, Surfaces, and Films,* **5** (4), 581-585 (1987).
31. J. A. Dumesic and A. A. Trevino, *Journal of Catalysis,* **116** 119-129 (1989).
32. B. Fastrup, *Journal of Catalysis,* **168** 235-244 (1997).
33. A. L. Garden and E. Skúlason, *The Journal of Physical Chemistry C,* **119** (47), 26554-26559 (2015).
34. C. D. Zeinalipour-Yazdi, J. S. J. Hargreaves, and C. R. A. Catlow, *The Journal of Physical Chemistry C,* **119** (51), 28368-28376 (2015).
35. I. A. Amar, R. Lan, C. T. G. Petit, and S. Tao, *International Journal of Electrochemical Science,* **10** (2015).
36. J. Díez-Ramírez, V. Kyriakou, I. Garagounis, A. Vourros, E. Vasileiou, P. Sánchez, F. Dorado, and M. Stoukides, *ACS Sustainable Chemistry & Engineering,* **5** (10), 8844-8851 (2017).
37. C. D. Zeinalipour-Yazdi, J. S. J. Hargreaves, and C. R. A. Catlow, *The Journal of Physical Chemistry C,* **122** (11), 6078-6082 (2018).
38. S. Back and Y. Jung, *Physical chemistry chemical physics : PCCP,* **18** (13), 9161-9166 (2016).
39. E. Skulason, T. Bligaard, S. Gudmundsdottir, F. Studt, J. Rossmeisl, F. Abild-Pedersen, T. Vegge, H. Jonsson, and J. K. Norskov, *Physical chemistry chemical physics : PCCP,* **14** (3), 1235-1245 (2012).
40. S. Trasatti, *Electroanalytical Chemistry and Interfacial Electrochemistry* **39** (1), 163-184 (1972).
41. J. K. Nørskov, T. Bligaard, A. Logadottir, J. R. Kitchin, J. G. Chen, S. Pandelov, and U. Stimming, *Journal of The Electrochemical Society,* **152** (3), J23 (2005).
42. K. Imamura and J. Kubota, *Sustainable Energy & Fuels,* **3** (6), 1406-1417 (2019).
43. X. Zhang, R. M. Kong, H. Du, L. Xia, and F. Qu, *Chemical communications,* **54** (42), 5323-5325 (2018).
44. P. Stoltze and J. K. Nørskov., *Journal of Catalysis,* **110** 1-10 (1988).
45. J. Qian, Q. An, A. Fortunelli, R. J. Nielsen, and W. A. Goddard, 3rd, *Journal of the American Chemical Society,* **140** (20), 6288-6297 (2018).
46. K. C. Waugh, *Catalysis Today,* **53** 161-176 (1999).
47. J. J. Mortensen, L. B. Hansen, B. Hammer, and J. K. Nørskov, *Journal of Catalysis,* **182** 479-488 (1999).
48. D. R. Strongin, J. Carrazza, S. R. Bare, and G. A. Somorjai, *Journal of Catalysis,* **103** 213-215 (1987).
49. G. A. Somorjai and N. Materer, *Topics in Catalysis,* **1** 215-231 (1994).
50. J. R. Anderson and M. Boudart, *Catalysis, Science and Technology Volume 4*, Springer-Verlag Berlin Heidelberg (1983).
51. K.-I. Aika, H. Hori, and A. Ozaki, *Journal of Catalysis,* **27** 424-431 (1972).
52. C. G. Vayenas and S. Brosda, *Topics in Catalysis,* **57** (14-16), 1287-1301 (2014).
53. D. Tsiplakides and C. G. Vayenas, *Journal of The Electrochemical Society,* **148** (5), E189 (2001).
54. C. G. Vayenas, S. Bebelis, and S. Ladas, *Nature,* **343** 625-627 (1990).
55. M. N. Tsampas, F. M. Sapountzi, and C. G. Vayenas, *Catalysis Today,* **146** (3-4), 351-358 (2009).
56. C. G. Vayenas, S. Bebelis, C. Pliangos, S. Brosda, and D. Tsiplakides, *Electrochemical Activation of Catalysis: Promotion, Electrochemical Promotion, and Metal-Support Interactions*, Kluwer Academic/Plenum Publishers (2001).

Effective electrode design and reaction mechanism for electrochemical promotion of ammonia synthesis using Fe-based electrode catalysts

Chien-I Li, Hiroki Matsuo and Junichiro Otomo

Effective electrode design is investigated and a very high ammonia formation rate via EPOC is achieved using Fe catalyst at high temperature.